photonics

MDPI

Article

Double-Layer Sandwich Metasurface for Mid-Infrared Multi-Channel Polarization Detection

Lifeng Ma [1], Yi Huang [1], Ting Zheng [1], Jun Chang [1,*] and Huilin Jiang [2]

[1] National Key Laboratory on Near-Surface Detection, School of Optics and Photonics, Beijing Institute of Technology, Beijing 100081, China; marryfeng7@163.com (L.M.); 3120225320@bit.edu.cn (Y.H.); 3120255558@bit.edu.cn (T.Z.)

[2] School of Optoelectronic Engineering, Changchun University of Science and Technology, Changchun 130022, China; 6120170045@bit.edu.cn

* Correspondence: optics_chang@126.com

Abstract

Conventional snapshot-type polarization devices often suffer from inherent ohmic losses caused by the metal structure, resulting in low utilization of system light energy. This research proposes a dual-layer sandwich architecture metasurface that integrates polarization control and high light transmittance for the mid-wave infrared 3~5 μm band. The top metal polarization-selective structures and the bottom dielectric hemispherical anti-reflection (AR) array are integrated monolithically on the same substrate. Specifically, the numerical simulations predict a peak transmittance of 95% at 4.4 and 4.8 μm, while maintaining extinction ratios ranging from 81.8 dB to 84.3 dB. This enables high extinction ratio polarization splitting while significantly broadening the transmittance flux of the device. It breaks the inherent trade-off between "high extinction ratio" and "high transmittance" in polarization devices, providing a high signal-to-noise ratio hardware foundation for high temporal resolution detection.

Keywords: sandwich architecture; metasurface; double-layer; high transmittance

1. Introduction

As an intrinsic property of light, polarization encodes a wealth of information regarding targets and their environments [1], including surface morphology [2], material composition [3], and atmospheric scattering characteristics [4]. Consequently, polarization imaging technology has been widely applied in fields such as remote sensing [5,6], biomedical diagnostics [7,8], and target tracking [5]. Among these, mid-wave infrared (MWIR) polarization imaging technology, by capturing both the thermal radiation and polarization characteristics of targets, can effectively enhance target recognition and anti-interference capabilities in complex backgrounds [9,10], demonstrating significant application value in environmental monitoring and security surveillance [11,12]. Among various implementation mechanisms, snapshot polarization imaging technology has emerged as a key technical approach for achieving high temporal resolution detection [13] due to its ability to simultaneously acquire multidimensional polarization information in a single exposure, making it particularly suitable for dynamic scene monitoring and high-speed target detection [14].

However, current mainstream snapshot polarization devices still primarily rely on metal subwavelength gratings. Constrained by the intrinsic ohmic losses of metallic materials and the Fresnel reflection effect at interfaces, such devices face issues such as low light energy utilization and insufficient transmittance flux in the mid-infrared band. This

Check for updates

Received: 16 June 2026
Revised: 16 July 2026
Accepted: 21 July 2026
Published: 27 July 2026

Copyright: © 2026 by the authors. Licensee MDPI, Basel, Switzerland. This article is an open access article distributed under the terms and conditions of the Creative Commons Attribution (CC BY) license.

results in a significant trade-off between polarization selectivity and transmittance, severely limiting further improvements in the system's signal-to-noise ratio (SNR) and temporal resolution [15,16]. Although traditional plasmonic polarizers can achieve extremely high extinction ratio (ER) by utilizing polarization-selective plasmonic responses, the severe intrinsic ohmic losses present in their metallic nanostructures [17–19] significantly reduce the device's transmitted power, leading to a sharp degradation in detection performance under low-light conditions. On the other hand, although all-dielectric alternatives can effectively suppress absorption losses, they often struggle to balance the compact physical dimensions required for pixel-level integration in imaging systems with high ER performance [20–22].

To address these issues, researchers worldwide have conducted extensive research: on the one hand, they have optimized the structural parameters of metallic gratings to reduce losses, but this still struggles to overcome the intrinsic absorption limitations of metallic materials [23]; on the other hand, all-dielectric polarization metasurfaces have been proposed to circumvent ohmic losses, yet their polarization ER and tuning flexibility remain difficult to match those of metallic devices [24,25]. Furthermore, existing devices largely rely on single-layer planar architectures, which lack effective suppression of interfacial reflection losses. This further exacerbates system light energy loss, making it difficult to meet the high light flux requirements of high temporal resolution polarization imaging. In recent years, metasurfaces composed of subwavelength artificial meta-atoms have garnered widespread attention due to their unique advantages in light-matter interactions at the nanoscale [26–28]. Despite significant progress in related research, developing a monolithic device that simultaneously achieves high ER and high transmittance remains a major challenge. The simple physical stacking of functional layers often leads to interlayer crosstalk or demanding manufacturing alignment challenges; therefore, there is an urgent need for a novel architectural design that decouples physical space from functionality.

In response to this research landscape, this study proposes a monolithic metasurface polarization device based on a double-layer sandwich architecture, effectively mitigating the conventional trade-off between ER and transmittance. The device employs a novel asymmetric double-layer design, monolithically integrating a top metallic polarization-selective layer and a bottom dielectric anti-reflection (AR) hemispherical layer onto a single dielectric substrate. In this design, the top layer consists of a custom-designed metal grating that acts as a highly selective polarization filter, ensuring excellent polarization extinction performance. Meanwhile, the bottom layer comprises an array of all-dielectric AR hemispheres that significantly suppress Fresnel reflection at the substrate exit surface, thereby improving optical coupling efficiency and enhancing overall transmittance flux. By ingeniously separating polarization selection from transmittance enhancement in both spatial and functional terms, this sandwich metasurface enhances the synergy between high ER and high optical transmittance. Deployed at the intermediate image plane of a mid-infrared cooled polarization imaging system, this monolithic, spatially decoupled photonic architecture not only opens up new avenues for micro-nano-scale polarization devices but also provides critical core component support for next-generation high temporal resolution mid-infrared polarization imaging systems.

2. Materials and Methods

This research proposes a double-layer sandwich architecture metasurface polarizing device for the MWIR polarization imaging system, as shown in Figure 1. This device integrates a metal polarization-selective structure and a dielectric hemispherical AR array onto the same substrate, decoupling the polarization selection process from the light field coupling enhancement process spatially, and achieving the collaborative optimization of polarization control and light transmittance while ensuring high polarization extinction

performance and enhancing optical throughput. This can provide a high-performance core component support for high-temporal-resolution infrared polarization detection.

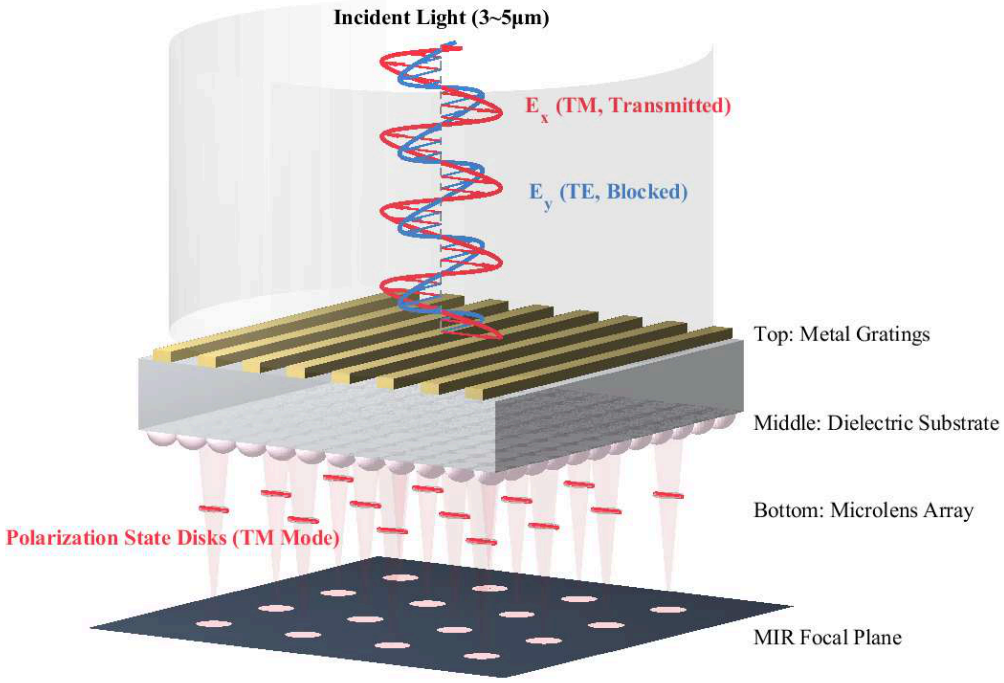


Figure 1. Schematic configuration of the sandwich architecture metasurface.

The device consists primarily of three layers: a top metallic subwavelength grating layer, a middle dielectric substrate layer, and a bottom AR array layer. The top metallic grating structure serves as the core functional layer responsible for polarization selectivity. Due to the strong anisotropic response of metallic subwavelength gratings to electromagnetic waves with different polarization directions, incident infrared light can be selectively transmitted based on polarization. When the incident electric field is perpendicular to the grating direction, electromagnetic waves effectively pass through the grating slits and transmit through, corresponding to the TM (Transverse Magnetic) polarization mode shown in the figure. Conversely, when the electric field is parallel to the metal grating, surface-induced currents are excited at the metal surface, resulting in significant reflection with accompanying ohmic absorption losses, thereby strongly suppressing the corresponding polarization component—this corresponds to the TE (Transverse Electric) polarization mode. Based on this polarization-selective effect, the device achieves high-extinction-ratio polarization separation. In the figure, red and blue spiral waveforms represent the electric field components along different polarization directions. The red electric field component E_x corresponds to the TM polarization mode that transmits through the device, while the blue E_y component represents the TE polarization mode suppressed by the metallic grating. Through this polarization selection mechanism, the device efficiently filters specific polarization states from incoming infrared light, enabling effective extraction of polarization information.

However, although conventional metallic polarization devices can achieve high polarization ER, their metallic structures inevitably suffer from ohmic losses, while dielectric interfaces introduce strong Fresnel reflections, leading to reduced overall transmittance efficiency and limiting system signal-to-noise ratio and dynamic detection capability. To maximize total optical throughput, the bottom layer of the device is designed as a dielectric hemispherical AR array facing the detector. The proposed dielectric hemispherical array can be regarded as a graded-index anti-reflection layer whose effective refractive index

varies continuously along the propagation direction. According to Effective Medium Theory (EMT), when the feature size is much smaller than the operating wavelength, the local effective refractive index can be approximated by

$$n_{\text{eff}}(z) = \sqrt{f(z)n_d^2 + (1 - f(z))n_a^2} \tag{1}$$

where n_d is the refractive index of the dielectric, $n_a = 1$ is the refractive index of air, $f(z)$ denotes the dielectric filling factor. For the hemispherical geometry,

$$f(z) = \frac{\pi r(z)^2}{P^2} \tag{2}$$

where $r(z) = \sqrt{R^2 - (R - z)^2}$. Consequently, the effective refractive index increases smoothly from approximately 1 to the substrate refractive index. Such a gradual index transition significantly suppresses Fresnel reflection according to $R = \left(\frac{n_2 - n_1}{n_2 + n_1}\right)^2$.

Instead of a single abrupt interface, the proposed hemispherical structure divides the substrate interface into numerous infinitesimal transitions, thereby greatly reducing impedance mismatch over the entire MWIR wavelength range. This broadband anti-reflection mechanism enables the metallic wire-grid to maintain its intrinsic polarization selectivity while substantially improving transmission efficiency.

This directional focusing not only further increases the effective optical flux absorbed by the detector but also greatly reduces optical crosstalk between adjacent pixels. Through synergistic effects of these two layers, the sandwich architecture spatially and functionally decouples the polarization selection process from the beam enhancement and focusing process, effectively overcoming the intrinsic trade-off between high ER and high transmittance commonly found in traditional single-layer polarization devices. This structure enhances the effective energy reception efficiency of detector pixels and further improves system optical throughput. This is significant for target recognition in low-light environments, dynamic thermal target monitoring, and infrared polarization detection in complex backgrounds.

The metasurface is deployed at the intermediate image plane of the polarization imaging system to achieve high temporal resolution snapshot polarization detection. As shown in Figure 2a, the designed polarization device adopts a novel monolithic asymmetric double-layer sandwich structure. The entire device is based on a silicon substrate, and the top grating adopts the meta-pixel design. To achieve snapshot polarization imaging, each meta-pixel contains four sub-pixels with different transmittance axis directions, and the grating arrangement direction is clockwise at 0°, 45°, 90° and 135°. Four polarization direction grating units are periodically spatially multiplexed and arranged, and the polarization direction of adjacent pixels rotates by 45° successively. Among them, the 0° and 90° direction gratings are mutually orthogonal, and the 45° and 135° direction gratings are also mutually orthogonal. This periodic spatial multiplexing arrangement ensures that the incident light beam can simultaneously sample four polarization projections within each meta-pixel, laying the physical foundation for subsequent snapshot demodulation. Since the polarization array must be used in conjunction with the detector, its unit size must be an integer multiple of the pixel unit size of the detector. After comprehensive consideration, the unit size of the polarization array is chosen to be the same as that of a single pixel unit, which is 15 μm. Between each pair of gratings in different polarization directions, a 1 μm-wide opaque area is reserved to reduce crosstalk between the polarization array and the detector units. After removing the reserved opaque area, the actual size of each unidirectional linear grating is 14 μm. There are 64 × 64 grating units, so the total area of the grating is 960 μm × 960 μm. Since this periodic polarization array can simultaneously

obtain the intensity information of different polarization directions during a single exposure, there is no need for traditional sequential scanning or mechanical rotation structures to simultaneously obtain polarization information, thereby significantly improving the system's temporal resolution and dynamic target detection capability.

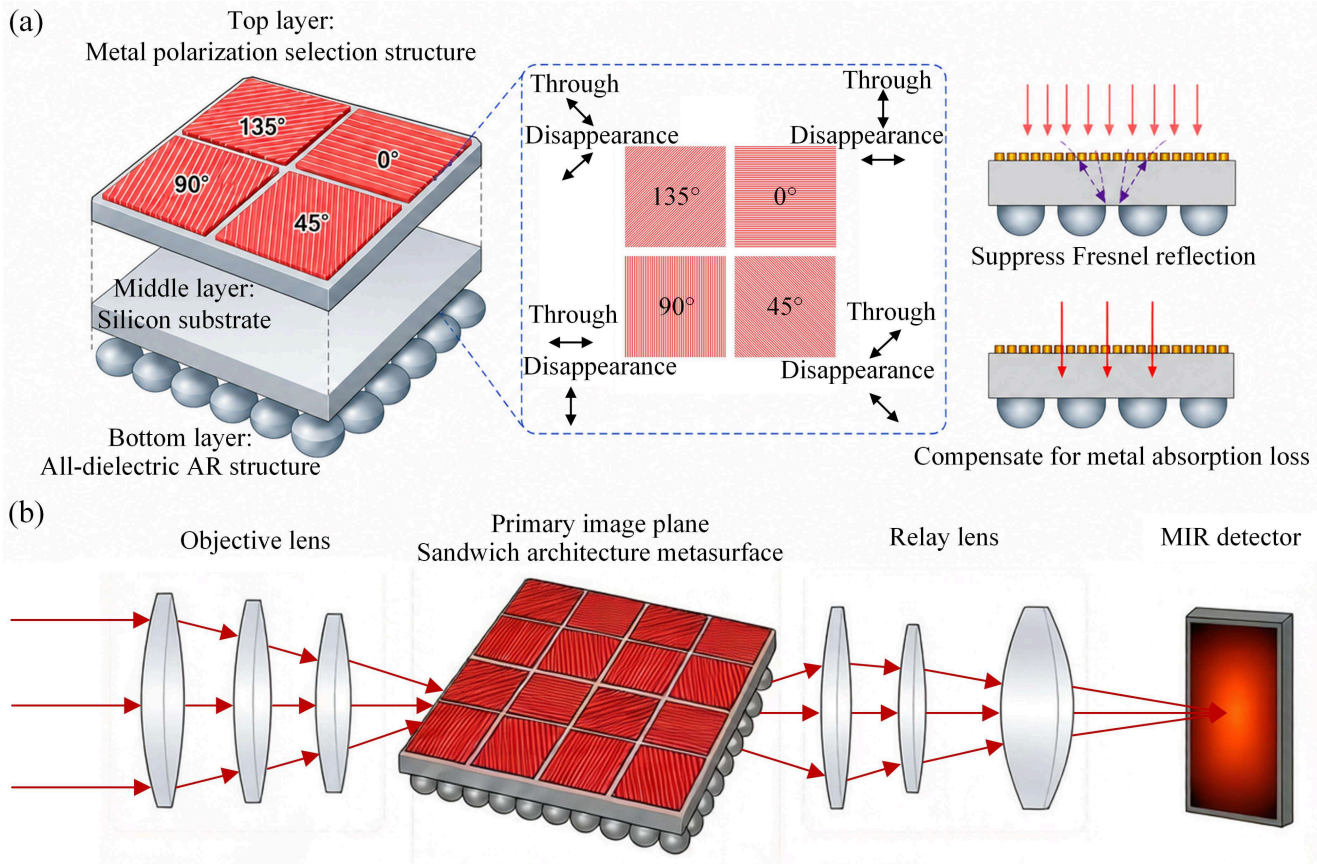


Figure 2. The working principle of the entire device. (**a**) The working principle of the metasurface. (**b**) The working principle of the optical system.

Figure 2b presents the working principle of the MWIR polarization imaging system based on this polarization metasurface. In the system, the MWIR radiation emitted by the target scene is first converged by the imaging objective and forms an intermediate image at the intermediate image plane. Then, the proposed double-layer sandwich architecture polarization metasurface is placed at the intermediate image plane position, and through its internal meta-pixel array with different polarization directions, the incident infrared image is spatially polarization-modulated. The metasurface is organized into a periodic superpixel configuration. Each superpixel consists of four neighboring pixels, whose metallic wire-grid orientations are designed as 0°, 45°, 90°, and 135°, respectively. Consequently, each subpixel independently measures one polarization component of the incident light. The four recorded intensity images are then used to reconstruct the first three Stokes parameters, thereby enabling snapshot polarization imaging without any mechanical scanning. Since all polarization channels are acquired simultaneously, the proposed architecture is particularly suitable for dynamic infrared scenes. Therefore, this double-layer sandwich architecture metasurface not only provides a new structural design idea for MWIR polarization devices but also provides important core component support for the next-generation high temporal resolution, high ER snapshot polarization imaging system.

The metallic wire-grid is designed to determine the polarization selectivity, whereas the dielectric hemispherical array mainly improves optical coupling through impedance

matching. Consequently, polarization discrimination and transmission enhancement are achieved by different structural components, allowing the two performance metrics to be optimized independently. This design philosophy differs fundamentally from conventional single-layer polarizers, where polarization filtering and transmission enhancement are intrinsically coupled. Furthermore, the proposed metasurface is developed for image-plane polarization modulation, which facilitates its integration into snapshot polarization imaging systems.

Due to the high number of structural degrees of freedom involved, including grating period, duty cycle, metal layer thickness, and AR film curvature radius, traditional parameter scanning methods relying on experience struggle to identify global optima within the vast solution space. Therefore, this study introduces particle swarm optimization (PSO) with an adaptive learning factor, deeply integrated with finite-difference time-domain (FDTD) physical simulation, enabling efficient co-optimization of micro-nano-structured AR parameters. As shown in Figure 3, the optimization process focuses on maximizing both the device's polarization ER and optical transmittance by jointly optimizing the parameters of the metallic grating structure and those of the bottom AR film's micro-nano architecture, achieving a high-performance design for MWIR polarization devices.

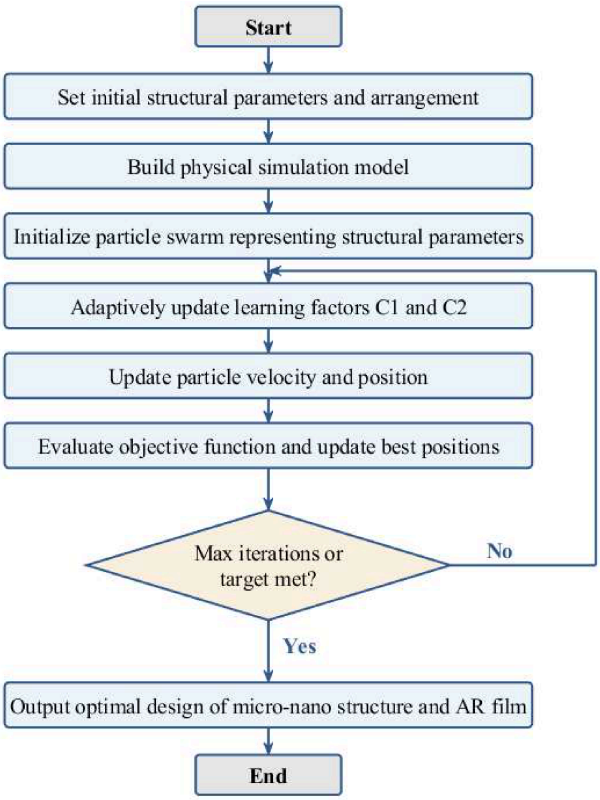


Figure 3. Flowchart for the optimization design of sandwich architecture metasurfaces.

Periodic boundary conditions were applied along the x- and y-directions to model an infinite periodic metasurface, whereas perfectly matched layers (PMLs) were employed along the propagation direction to eliminate artificial reflections. A linearly polarized plane wave was normally incident onto the metasurface, covering the wavelength range from 3 μm to 5 μm. The transmission and reflection spectra were recorded using frequency-domain power monitors positioned above and below the metasurface. The optical constants of aluminum, silicon dioxide and silicon were directly imported from the dispersive material database implemented in the simulation software. A mesh override region was introduced around the metallic grating, and a sufficiently fine mesh was adopted to ensure

numerical convergence. The simulation was terminated automatically once the residual electromagnetic energy fell below the preset convergence threshold. The specific simulation data are shown in Table 1.

Table 1. Settings for conditions and parameters during the simulation process.

Parameter	Value
Wavelength Range	3–5 μm
Source	Plane Wave
Polarization	TE/TM
Boundary (x,y)	Periodic
Boundary (z)	PML
Mesh Type	Mesh Override
Minimum Mesh Size	0.25 nm
Auto Shutoff	1×10^{-5}
Transmission Monitor	Below Structure
Reflection Monitor	Above Source
Material	Dispersive Al/Si/SiO_2

As illustrated in Figure 3, the entire optimization process begins with defining the initial structural parameters of the device. Based on the MWIR operating wavelength range and subwavelength polarization grating theory, initial ranges are pre-assigned for key parameters such as grating period, linewidth, thickness, duty cycle, dielectric substrate thickness, and the radius of the AR hemispherical layer at the bottom. Simultaneously, the spatial arrangement of four-directional polarization units and the periodic array configuration are determined, establishing the foundation for subsequent parametric modeling. Subsequently, a complete electromagnetic simulation model is constructed according to the device's physical structure. In this work, FDTD is employed to solve Maxwell's equations, analyzing the polarization transmittance characteristics of the device in the MWIR. During the optimization process, the structural parameters of the device are encoded as particles within the particle swarm. Each particle corresponds to a complete set of structural design parameters, including grating period, duty cycle, metal thickness, and hemisphere radius. After initialization, each particle corresponds to an independent electromagnetic simulation model, and its associated polarization performance metrics are calculated.

To simultaneously achieve high transmittance and high ER, a multi-objective optimization function is formulated. The polarization ER of the device is defined as:

$$ER = 10 \log_{10}\left(\frac{T_{TM}}{T_{TE}}\right) \tag{3}$$

where T_{TM} represents the transmittance for TM polarization and T_{TE} represents the transmittance for TE polarization. Considering the high ER and high optical flux requirements of the device, a combined objective function is established:

$$F = \alpha \cdot ER + \beta \cdot T_{TM} \tag{4}$$

Among them, α and β are dimensionless weight coefficients used to balance the optimization requirements of polarization performance and transmittance. The standard PSO is prone to getting stuck in local optima in complex multi-peak electromagnetic field optimization problems. Therefore, this process introduces personal learning coefficient c_1 and global learning coefficient c_2 that dynamically adjust linearly with the number of iterations. Assuming the current iteration number is *iter* and the maximum set iteration

number is $iter_{max}$, the adaptive update mechanism of the learning factor follows the following mathematical rule:

$$C_1 = C_{1,min} + (C_{1,max} - C_{1,min}) \times \left(\frac{iter}{iter_{max}} \right) \tag{5}$$

$$C_2 = C_{2,min} + (C_{2,max} - C_{2,min}) \times \left(1 - \frac{iter}{iter_{max}} \right) \tag{6}$$

Under this mechanism, as the iterations proceed, C_1 gradually increases while C_2 gradually decreases. This indicates that in the initial stage of the search, the particle swarm exhibits strong social conformity, capable of rapidly converging towards the global advantageous area and narrowing the search scope; while in the later iterations, the particles rely more on their own individual experience and conduct refined searches within the local area, effectively avoiding premature convergence caused by population convergence and improving the probability of finding the global optimal micro-nano structure. During the particle swarm iteration process, the particle positions and velocities are dynamically updated based on the global optimal solution and individual optimal solution. The velocity update formula for the particles is:

$$v_i^{k+1} = \omega v_i^k + C_1 r_1 \left(p_i^k - x_i^k \right) + C_2 r_2 \left(g^k - x_i^k \right) \tag{7}$$

The formula for updating the particle position is:

$$x_i^{k+1} = x_i^k + v_i^{k+1} \tag{8}$$

Among them, x_i^k and v_i^k represent the position and velocity of the i-th particle at the k-th iteration respectively; p_i^k represents the individual historical optimal position; g^k represents the global optimal position; C_1 and C_2 are the individual learning factor and the group learning factor respectively; r_1 and r_2 are random numbers between 0 and 1; ω is the inertia weight.

To enhance the global search ability of the algorithm and avoid early convergence to the local optimum, this paper further adopts an adaptive learning factor update strategy. In the early stage of optimization, the global search ability is improved so that the particles can quickly traverse the parameter space; in the later stage, the local search ability is enhanced to improve the convergence accuracy of the optimal solution. After each position update is completed, the new parameter combination x_i^k is re-substituted into the physical optics simulation software for strict electromagnetic field calculation, new T_{TM} and T_{TE} are extracted, and the current objective function value F is calculated. The algorithm conducts convergence checks at the end of each cycle. When the number of iterations reaches the preset maximum value $iter_{max}$, or the continuous change in the global optimal objective function value of the population for multiple generations is less than the set minimum threshold, that is, when the required high transmittance and ER requirements are met, the optimization process terminates; otherwise, the algorithm returns and continues to calculate and update the adaptive factors and positions for the next round. When the algorithm successfully converges and stops running, the system extracts the current global optimal solution.

3. Results

The complete structural parameters of the proposed double-layer sandwich metasurface are summarized in Table 2. The device consists of a metallic wire-grid polarizer fabricated on the upper surface of a silicon substrate, while a dielectric hemispherical

anti-reflection array is patterned on the opposite surface. All geometrical parameters used in the FDTD simulations are listed.

Table 2. All the geometric parameters used in the simulation.

Parameter	Symbol	Value	Unit
Wire-grid period	P_g	340	nm
Wire width	W	170	nm
Duty cycle	$D = W/P_g$	0.5	-
Metal thickness	H_m	440	nm
Hemisphere radius	R	250	nm
Hemisphere height	H_h	300	nm
Conical coefficient	C_h	-1	-
Curvature radius	R_h	0.1	-
Base thickness	H_b	6000	nm

Figure 4 illustrates the variation in the transmittance and ER of the device with wavelength. The red curve with solid squares represents the transmittance. A prominent feature of the spectral response is the presence of pronounced periodic oscillations across the investigated wavelength range. Several resonant peaks are observed, with the transmittance approaching 95% near 4.4 μm and 4.8 μm. At these wavelengths, the ER simultaneously exceeds 80 dB, indicating excellent polarization discrimination while maintaining high optical throughput. The periodic oscillations observed in the transmission spectra originate from Fabry–Perot resonances established inside the silicon substrate. As the incident wavelength varies, the round-trip optical phase continuously changes, leading to alternating constructive and destructive interference. At resonance wavelengths, destructive interference of the reflected waves minimizes the overall reflection, thereby maximizing the transmitted optical power. Since the metallic wire-grid strongly suppresses TE-polarized transmission over the entire wavelength range, the extinction ratio mainly follows the variation in the TM transmission. Consequently, both transmission and extinction ratios reach their maxima at approximately the same resonance wavelengths.

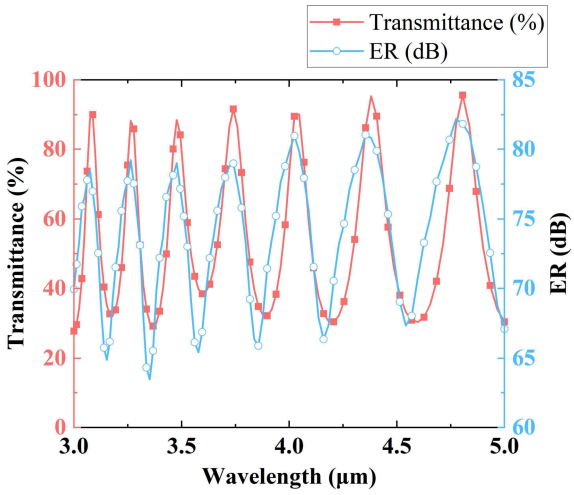


Figure 4. The simulation results of transmittance and ER.

Notably, the transmittance and ER spectra exhibit highly consistent variation trends. Regions of enhanced transmittance generally coincide with elevated ER values, suggesting that the resonant modes contribute simultaneously to transmission enhancement and polarization selectivity. Such behavior effectively alleviates the conventional trade-off between optical throughput and extinction ratio that is commonly encountered in traditional

polarization devices. Although the spectral response exhibits resonance-induced comb-like oscillations rather than a perfectly flat broadband characteristic, the device maintains high transmittance and strong polarization extinction across multiple wavelength regions of interest. These wavelength-selective enhancement characteristics are particularly attractive for multispectral polarization sensing and target detection applications, where high signal throughput and strong polarization contrast are required simultaneously.

To better position our results within the current state-of-the-art, we have compared the key performance metrics of our proposed structure with several recently reported bilayer or hybrid wire-grid polarizers designed for the MWIR. As summarized in Table 3, while prior works have demonstrated high ER, their transmittance is often constrained by absorption or reflection losses inherent to planar high-index substrates. In contrast, the double-layer sandwich architecture introduced in this work achieves a superior balance. The proposed device reaches a peak transmittance of 95% at 4.4 and 4.8 μm while maintaining an ER exceeding 81 dB across the 3–5 μm range.

Table 3. Simulation performance comparison with state-of-the-art MWIR polarization devices.

Reference Work	Jeon et al. [29]	Kong et al. [30]	Liu et al. [31]	Our Work
Design method	Finite integration technique	FDTD	FDTD	FDTD + PSO with adaptive learning factors
Wavelength	3~5 μm	1~5 μm	3~5 μm	3~5 μm
Structure	Bilayer wire-grid	Metal–dielectric–Pmetal	Au–Pt–Ti wire-grid	double-layer sandwich architecture
Transmittance	>90%	89%@4 μm	Maximum 74.2%	Maximum 95%@4.4 μm and 4.8 μm
ER	40.8 dB@3.5 μm 42.3 dB@4.5 μm	42 dB@4 μm	28.68 dB@3.89 μm 2.77 dB@4.57 μm	81.8~84.3 dB

Figure 5 compares the calculated reflection spectra of the proposed structure with and without the dielectric hemispherical layer over the 3–5 μm wavelength range. Both structures exhibit periodic spectral oscillations, indicating that the reflection characteristics are strongly influenced by multiple-beam interference inside the multilayer structure. The oscillation period remains nearly unchanged after introducing the hemispherical layer, suggesting that the additional dielectric layer does not alter the fundamental resonance condition but mainly affects the coupling efficiency at the air–substrate interface.

Compared with the conventional planar structure, the introduction of the hemispherical dielectric array leads to a noticeable reduction in reflection across the entire operating band. The difference is particularly evident near the resonance wavelengths, where the reflectivity decreases by several percentage points. The reduction in reflection can be attributed to the gradual refractive-index transition introduced by the hemispherical geometry. Instead of an abrupt refractive-index discontinuity between air and silicon, the hemispherical profile provides a smoother impedance transition, thereby reducing interface reflections over a broad wavelength range. As a result, a larger fraction of the incident optical energy is coupled into the substrate and subsequently transmitted through the metallic grating.

It is also observed that the reflection minima coincide with the transmission maxima reported in Figure 4. This complementary behavior satisfies the energy conservation relationship of the optical system and further confirms that the enhanced transmission originates primarily from reduced reflection losses. Since the metallic absorption remains

nearly unchanged after introducing the dielectric hemispherical layer, the improvement in optical throughput is mainly associated with the suppression of interface reflection.

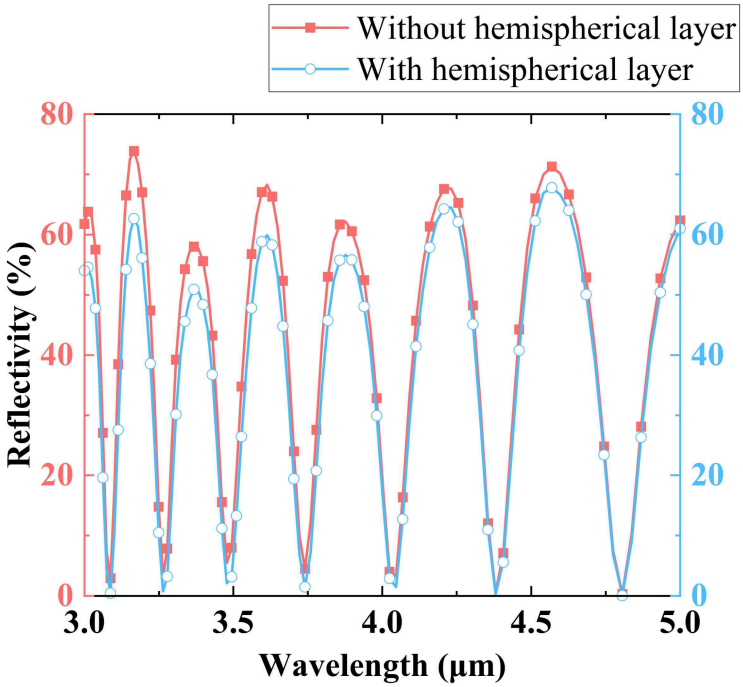


Figure 5. The reflection spectra with and without the hemispherical layer.

Figure 6 presents the angular dependence of the transmittance and ER of the proposed metasurface device for incident angles ranging from 0° to 30°. Both curves remain nearly flat throughout the investigated angular range, indicating excellent angular stability and wide-angle operating capability. This characteristic is particularly important for practical MWIR polarization imaging systems, where chief rays originating from different field positions generally impinge on the polarization element with varying incident angles. Excessive angular sensitivity would lead to spatially nonuniform polarization responses and degrade the accuracy of polarization reconstruction. Therefore, maintaining stable transmittance and ER over a wide angular range is essential for high-fidelity polarization imaging.

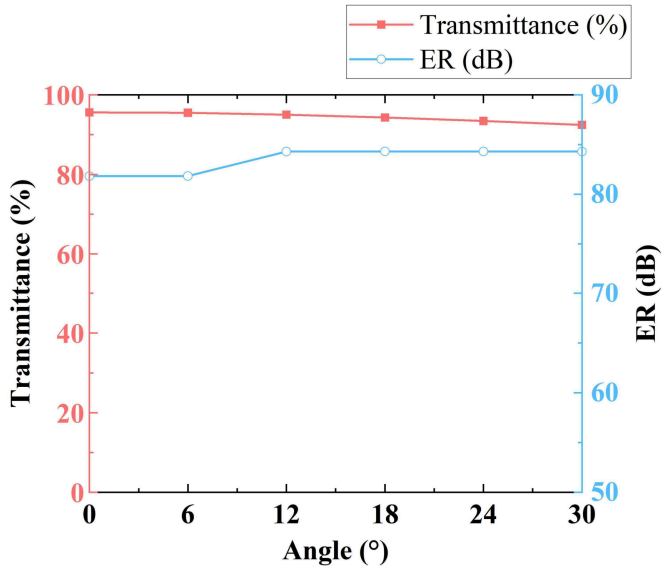


Figure 6. The varying transmittance and ER with the change in angle.

The red curve with solid squares shows the transmittance of the device at a wavelength of 4.8 μm as a function of incident angle. Throughout the investigated range, the transmittance remains above 92%, exhibiting fluctuations of less than 4%. Specifically, as the incident angle increases from 0° to 30°, the transmittance remains within the narrow range of approximately 92–96%, indicating low insertion loss and efficient optical throughput. This behavior can be attributed to the synergistic effect of the double-layer sandwich architecture. The top metallic subwavelength grating provides stable polarization selection, while the bottom dielectric hemispherical AR array suppresses interface reflections and enhances optical coupling efficiency. Consequently, the device maintains high transmittance performance even under oblique incidence. The proposed metasurface exhibits stable optical performance for incident angles up to approximately 30°. Typical MWIR imaging systems generally operate with numerical apertures corresponding to chief-ray angles well below 30°. The F-number of the lens is 2. Then, $NA = \frac{1}{2F} = 0.25$, and the corresponding maximum angle $\theta = arcsin(NA) \approx 14°$.Therefore, the angular range investigated in the present work already covers the practical operating conditions of most infrared polarization imaging systems.

The blue curve with open circles represents the ER as a function of incident angle. The ER consistently exceeds 81 dB over the entire angular range, varying only slightly between approximately 81.8 dB and 84.3 dB. Such behavior demonstrates excellent angular robustness of the polarization selectivity. The absence of noticeable degradation in either transmittance or ER suggests that higher-order diffraction and mode-coupling effects remain effectively suppressed within the investigated angular range. Since the grating period is significantly smaller than the operating wavelength, the structure remains in the subwavelength regime, where zero-order transmittance dominates the optical response. In addition, the dielectric hemispherical AR array provides a gradual refractive index transition that mitigates angle-dependent Fresnel reflections.

Overall, the minimal variation observed in both transmittance and ER confirms the excellent angular tolerance of the proposed sandwich-architecture polarization metasurface. Such angular robustness is highly desirable for large-field-of-view MWIR polarization imaging systems, where consistent polarization performance across different field positions is required. The results demonstrate that the proposed device can simultaneously maintain high transmittance and high ER over a wide angular range, highlighting its potential for high-performance infrared polarization imaging applications.

To further evaluate the applicability of the proposed metasurface in polarization imaging, a numerical imaging demonstration was carried out. As shown in Figure 7, a synthetic polarization scene containing different polarization orientations was generated as the input target. After passing through the proposed metasurface, four polarization intensity images corresponding to different analysis channels were obtained. Based on these recorded intensities, the Stokes parameters were reconstructed according to

$$\begin{aligned} S_0 &= I_{0^\circ} + I_{90^\circ} \\ S_1 &= I_{0^\circ} - I_{90^\circ} \\ S_2 &= I_{45^\circ} - I_{135^\circ} \end{aligned} \tag{9}$$

The Degree of Linear Polarization (DoLP) was then calculated by $DoLP = \frac{\sqrt{S_1^2+S_2^2}}{S_0}$, while the Angle of Linear Polarization (AoLP) was determined by $AoLP = \frac{1}{2}\tan^{-1}\left(\frac{S_2}{S_1}\right)$. This demonstrates the feasibility of the proposed metasurface for snapshot polarization imaging.

To elucidate the microscopic physical mechanism of the polarization filtering, the near-field intensity distributions $|E|^2$ and $|H|^2$ of the composite metasurface were investigated at two typical mid-infrared wavelengths, 4.4 μm and 4.8 μm.

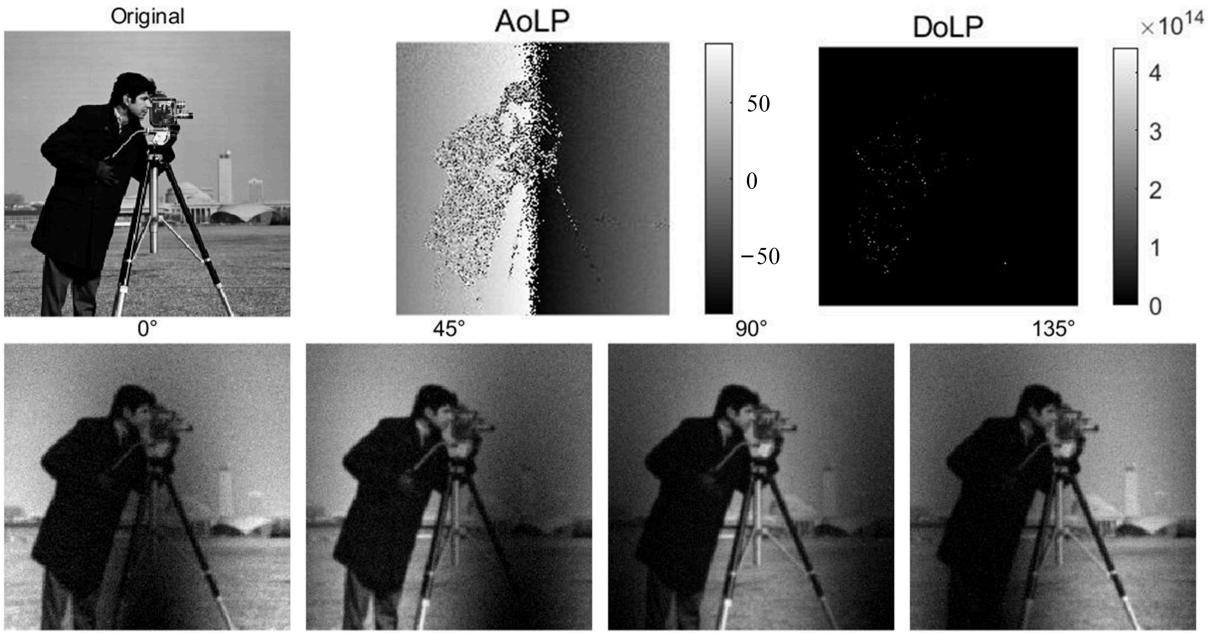


Figure 7. Demonstration of analog numerical imaging of the device.

For the TM incidence (Figure 8c,d,g,h), the structure demonstrates remarkable forward coupling. The maximum electric field intensity $|E|^2$ reaches approximately 0.49 to 0.53. In sharp contrast, when the incident light switches to the TE polarization (Figure 8a,b,e,f), the subwavelength Al grating behaves in a strict cut-off regime. Observing the color bar scales, the field intensities of the TE mode are drastically suppressed to the order of 10^{-9}, which is nearly eight orders of magnitude lower than that of the TM mode. Such a massive contrast in field localization visually and quantitatively corroborates the ultra-high extinction ratio achieved by this device. Furthermore, the spatial uniformity of the field distributions remains highly consistent at both 4.4 μm and 4.8 μm, verifying the broadband stability of the proposed sandwich architecture across the 3–5 μm band.

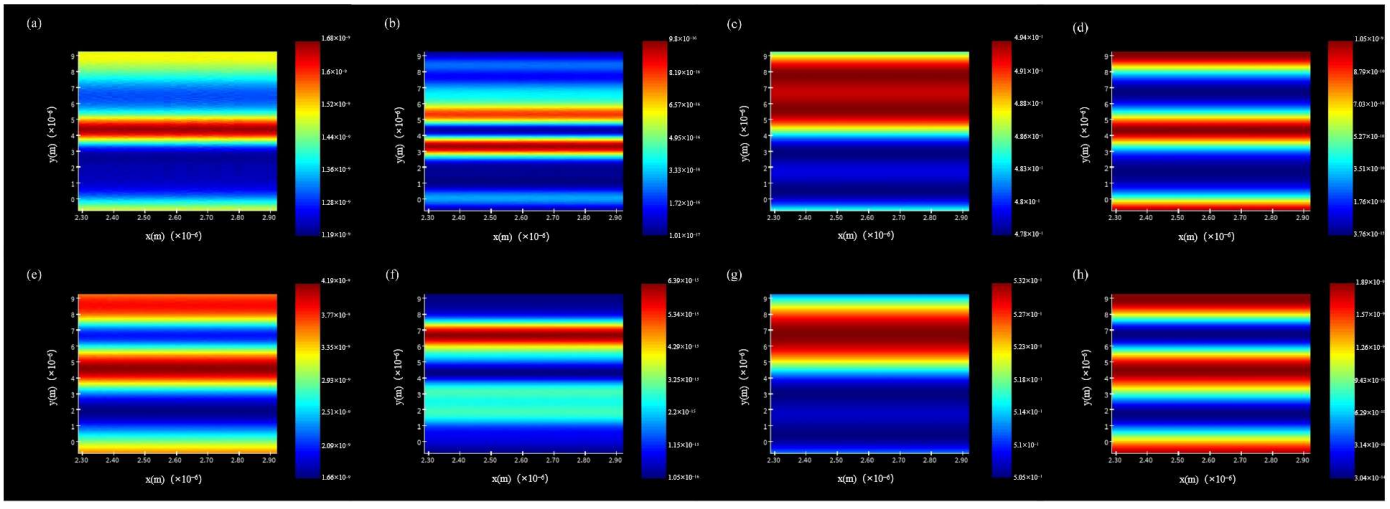


Figure 8. Near-field electromagnetic distributions of the metasurface: At 4.4 μm, (**a**) the electric field $|E|^2$ obtained and (**b**) the magnetic field $|H|^2$ obtained after TE-polarized light incidence, (**c**) the electric field $|E|^2$ obtained and (**d**) the magnetic field $|H|^2$ obtained after TM-polarized light incidence. At 4.8 μm, (**e**) the electric field $|E|^2$ obtained and (**f**) the magnetic field $|H|^2$ obtained after TE-polarized light incidence, (**g**) the electric field $|E|^2$ and (**h**) the magnetic field $|H|^2$ obtained after TM-polarized light incidence.

The influence of fabrication imperfections was investigated by introducing dimensional variations into the optimized structure. As is shown in Figure 9, the simulation results indicate that the transmission and extinction ratio exhibit only limited degradation under moderate dimensional deviations, demonstrating that the proposed structure possesses satisfactory fabrication robustness.

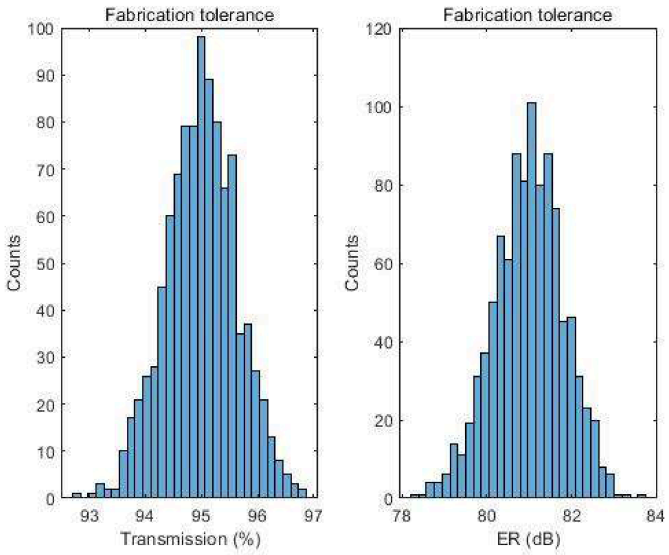


Figure 9. The transmission and ER obtained by introducing fabrication deviations.

The proposed metasurface is composed of aluminum, silicon and silicon dioxide, both of which exhibit excellent thermal stability in the MWIR spectral region. Although the refractive index of silicon slightly varies with temperature, the corresponding resonance wavelength shift is relatively small, and therefore the optical performance remains nearly unchanged under typical operating conditions. Consequently, the proposed device is expected to operate reliably in practical infrared imaging systems.

To verify the numerical accuracy, mesh convergence tests were performed by gradually refining the computational mesh. As is shown in Figure 10, the extinction ratio rapidly converged as the mesh size decreased, indicating that the reported performance is not caused by numerical discretization errors. The final simulations were carried out using a sufficiently fine mesh, where further refinement resulted in negligible variations.

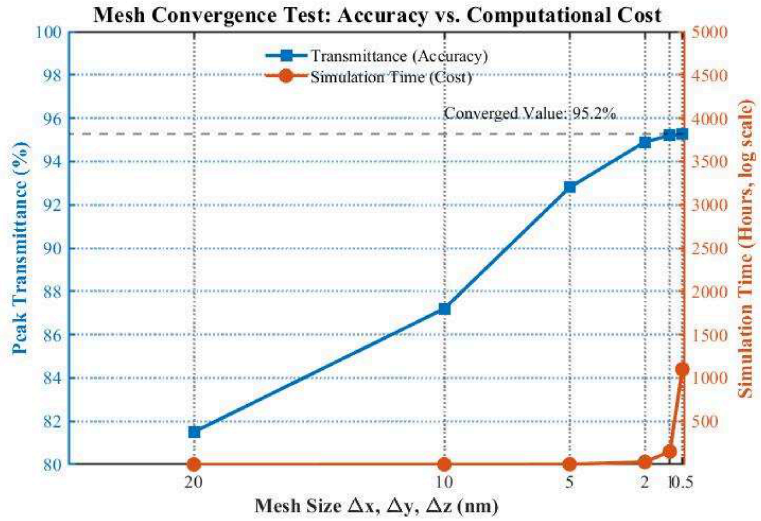


Figure 10. The variation in transmission and simulation time with the convergence of the mesh.

The reliability of the proposed metasurface has been assessed through several complementary numerical analyses. Reflection spectra demonstrate that the enhanced transmission originates from effective suppression of Fresnel reflection. Near-field electromagnetic distributions reveal the energy localization inside the dielectric substrate, confirming the physical mechanism of transmission enhancement. Mesh convergence tests indicate that the calculated transmission and extinction ratio remain nearly unchanged under further mesh refinement, confirming numerical stability. Fabrication tolerance analysis and polarization imaging simulations further demonstrate the robustness and practical applicability of the proposed design.

4. Conclusions

From the perspective of the application of polarization imaging systems, this result indicates that the proposed double-layer sandwich metasurface polarization device not only has high transmittance and a high extinction ratio but also can maintain stable performance within a wide range of incident angles. This is particularly important for MWIR polarization imaging systems with a large field of view. During the actual imaging process, the incident angles of the chief rays corresponding to different field-of-view positions usually vary, and the device's excellent angle tolerance can ensure a consistent polarization response throughout the field of view, thereby improving the accuracy of Stokes parameter reconstruction and the quality of polarization images. In addition, the higher and more stable transmittance also helps to improve the system's signal-to-noise ratio and the ability to detect weak targets. Overall, at 4.8 μm, within the range of 0–30°, this device was numerically predicted to provide a transmittance greater than 92% and an extinction ratio higher than 81.8 dB, fully verifying the effectiveness of the double-layer sandwich structure design in enhancing the angle robustness of mid-wave infrared polarization devices and providing a solid foundation for the engineering application of subsequent large-field-of-view, high-time-resolution polarization imaging systems.

Author Contributions: Conceptualization, L.M. and Y.H.; methodology, L.M.; software, L.M.; validation, Y.H.; formal analysis, L.M.; investigation, L.M.; resources, H.J.; data curation, L.M.; writing—original draft preparation, L.M.; writing—review and editing, Y.H.; visualization, T.Z.; supervision, J.C.; project administration, J.C.; funding acquisition, J.C. All authors have read and agreed to the published version of the manuscript.

Funding: This research received no external funding.

Institutional Review Board Statement: Not applicable.

Data Availability Statement: No new data were created or analyzed in this study. Data sharing is not applicable to this article.

Conflicts of Interest: The authors declare no conflicts of interest.

Abbreviations

The following abbreviations are used in this manuscript:

ER	extinction ratio
AR	anti-reflective
FDTD	finite-difference time-domain
MWIR	mid-wave infrared
PSO	particle swarm optimization
PMLs	perfectly matched layers

References

1. Chen, H.; Wolff, L.B. Polarization Phase-Based Method For Material Classification in Computer Vision. *Int. J. Comput. Vis.* **1998**, *28*, 73–83. [CrossRef]
2. Aspnes, D.E.; Studna, A.A. High precision scanning ellipsometer. *Appl. Opt.* **1975**, *14*, 220–228. [CrossRef] [PubMed]
3. Sun, T.; Liu, T.; He, H.; Wu, J.; Ma, H. Distinguishing anisotropy orientations originated from scattering and birefringence of turbid media using Mueller matrix derived parameters. *Opt. Lett.* **2018**, *43*, 4092–4095. [CrossRef] [PubMed]
4. Mishchenko, M.I.; Travis, L.D. Satellite retrieval of aerosol properties over the ocean using polarization as well as intensity of reflected sunlight. *J. Geophys. Res.* **1997**, *102*, 16989–17013. [CrossRef]
5. Tyo, J.S.; Goldstein, D.L.; Chenault, D.B.; Shaw, J.A. Review of passive imaging polarimetry for remote sensing applications. *Appl. Opt.* **2006**, *45*, 5453–5469. [CrossRef] [PubMed]
6. Moran, T.G.; Davila, J.M. Three-Dimensional Polarimetric Imaging of Coronal Mass Ejections. *Science* **2004**, *305*, 66–70. [CrossRef] [PubMed]
7. Gurjar, R.S.; Backman, V.; Perelman, L.T.; Georgakoudi, I.; Badizadegan, K.; Itzkan, I.; Dasari, R.R.; Feld, M.S. Imaging human epithelial properties with polarized light-scattering spectroscopy. *Nat. Med.* **2001**, *7*, 1245–1248. [CrossRef] [PubMed]
8. He, C.; He, H.; Chang, J.; Chen, B.; Ma, H.; Booth, M.J. Polarisation optics for biomedical and clinical applications: A review. *Light Sci. Appl.* **2021**, *10*, 194. [CrossRef] [PubMed]
9. Cremer, F.; de Jong, W.; Schutte, K. Infrared polarisation measurements of surface and buried anti-personnel landmines. In Proceedings of the Detection and Remediation Technologies for Mines and Minelike Targets VI, Orlando, FL, USA, 16–20 April 2001.
10. Woolley, M.; Michalson, J.; Romano, J. Observations on the polarimetric imagery collection experiment database. In Proceedings of the Polarization Science and Remote Sensing V, Bellingham, WA, USA, 21–22 August 2011.
11. Rubin, N.A.; D'aversa, G.; Chevalier, P.; Shi, Z.; Chen, W.T.; Capasso, F. Matrix Fourier optics enables a compact full-Stokes polarization camera. *Science* **2019**, *365*, eaax1839. [CrossRef] [PubMed]
12. Zhan, Z.; Cantono, M.; Kamalov, V.; Mecozzi, A.; Müller, R.; Yin, S.; Castellanos, J.C. Optical polarization-based seismic and water wave sensing on transoceanic cables. *Science* **2021**, *371*, 931–936. [CrossRef] [PubMed]
13. Gruev, V.; Perkins, R.; York, T. CCD polarization imaging sensor with aluminum nanowire optical filters. *Opt. Express* **2010**, *18*, 19087–19094. [CrossRef] [PubMed]
14. Yang, B.; Lee, P.; Hua, Y.; Brazile, B.; Waxman, S.; Ji, F.; Zhu, Z.; Sigal, I.A. Instant polarized light microscopy for imaging collagen microarchitecture and dynamics. *J. Biophotonics* **2021**, *14*, e202000326. [PubMed]
15. Yamada, I.; Yamashita, N.; Tani, K.; Einishi, T.; Saito, M.; Fukumi, K.; Nishii, J. Fabrication of a mid-IR wire-grid polarizer by direct imprinting on chalcogenide glass. *Opt. Lett.* **2011**, *36*, 3882–3884. [CrossRef] [PubMed]
16. Yuan, W.; Tian, S.; Guo, J.; Chen, Y. Multilayer subwavelength metallic grating as a high performance polarizer in infrared short wavelengths. *Opt. Lett.* **2024**, *49*, 6793–6796. [CrossRef] [PubMed]
17. Khurgin, J.B. How to deal with the loss in plasmonics and metamaterials. *Nat. Nanotechnol.* **2015**, *10*, 2–6. [CrossRef] [PubMed]
18. Chen, B.; Fu, X.; Liu, X.; Pan, Y.; Dong, S.; Wang, B.; Lin, Z.; Jiang, H. A Review of Sub-Wavelength Wire Grid Polarizers and Their Development Trends. *Photonics* **2025**, *12*, 1046. [CrossRef]
19. Qin, F.; Ding, L.; Zhang, L.; Monticone, F.; Chum, C.C.; Deng, J.; Mei, S.; Li, Y.; Teng, J.; Hong, M.; et al. Hybrid bilayer plasmonic metasurface efficiently manipulates visible light. *Sci. Adv.* **2016**, *2*, e1501168. [CrossRef] [PubMed]
20. Arbabi, A.; Arbabi, E.; Horie, Y.; Kamali, S.M.; Faraon, A. Planar metasurface retroreflector. *Nat. Photonics* **2017**, *11*, 415–420. [CrossRef]
21. Hu, Y.; Wang, X.; Luo, X.; Ou, X.; Li, L.; Chen, Y.; Yang, P.; Wang, S.; Duan, H. All-dielectric metasurfaces for polarization manipulation: Principles and emerging applications. *Nanophotonics* **2020**, *9*, 3755–3780. [CrossRef]
22. Yan, C.; Li, X.; Pu, M.; Ma, X.; Zhang, F.; Gao, P.; Liu, K.; Luo, X. Midinfrared real-time polarization imaging with all-dielectric metasurfaces. *Appl. Phys. Lett.* **2019**, *114*, 161904. [CrossRef]
23. Lee, J.; Oh, J.; Chi, H.; Lee, M.; Hwang, J.; Jeong, S.; Kang, S.; Jee, H.; Bae, H.; Hyun, J.; et al. Deep Learning-Assisted Design of Bilayer Nanowire Gratings for High-Performance MWIR Polarizers. *Adv. Mater. Technol.* **2024**, *9*, 2302176. [CrossRef]
24. Jahani, S.; Jacob, Z. All-dielectric metamaterials. *Nat. Nanotechnol.* **2016**, *11*, 23–36. [CrossRef] [PubMed]
25. Kuznetsov, A.I.; Miroshnichenko, A.E.; Brongersma, M.L.; Kivshar, Y.S.; Luk'yanchuk, B. Optically resonant dielectric nanostructures. *Science* **2016**, *354*, aag2472. [CrossRef] [PubMed]
26. Yu, N.; Capasso, F. Flat optics with designer metasurfaces. *Nat. Mater.* **2014**, *13*, 139–150. [CrossRef] [PubMed]
27. Kildishev, A.V.; Boltasseva, A.; Shalaev, V.M. Planar photonics with metasurfaces. *Science* **2013**, *339*, 1232009. [CrossRef] [PubMed]
28. Zhang, Z.; Li, L.; Tang, T.; Zhang, F.; Du, A.; Pu, M.; Kang, T.; Guo, Y.; Yang, J.; Luo, X. Broadband polarization-asymmetric directional thermal emission enabled by opposite phase-gradient metasurfaces. *PhotoniX* **2026**, *7*, 41. [CrossRef]
29. Jeon, J.; Chun, B.S.; Seo, Y.; Kim, M.; Kim, H.; Kim, Y.; Kim, J.S.; Lee, S.J. Improving infra-red polarized imaging efficiency in a bilayer wire-grid polarizer. *Nanoscale Adv.* **2023**, *5*, 633–639. [CrossRef] [PubMed]

30. Kong, Y.; Liu, D.; Luo, H. Effect of magnetic polaritons on the polarization characteristics of metal–dielectric–metal infrared wire-grid polarizers. *Opt. Commun.* **2020**, *474*, 126111. [CrossRef]
31. Liu, S.-H.; Zhao, Z.-J.; Xu, F.-Y.; Xu, S.-C.; Gong, X.-X.; Fan, M.-G.; Luo, Y.-F.; Qing, H.-Y. Design of an Au–Pt–Ti wire-grid polarizer based on midinfrared pixelated micropolarizer arrays. *Opt. Eng.* **2023**, *62*, 037104. [CrossRef]

Disclaimer/Publisher's Note: The statements, opinions and data contained in all publications are solely those of the individual author(s) and contributor(s) and not of MDPI and/or the editor(s). MDPI and/or the editor(s) disclaim responsibility for any injury to people or property resulting from any ideas, methods, instructions or products referred to in the content.